Bioderived ether design for low soot emission and high reactivity transport fuels

Jaeyoung Cho[1,†], Yeonjoon Kim[2,†], Brian D. Etz[1], Gina M. Fioroni[1], Nimal Naser[1], Junqing Zhu[3], Zhanhong Xiang[3], Cameron Hays[1], Juanvi Alegre Requena[2], Peter C. St John[1], Bradley T. Zigler[1], Charles S. McEnally[3], Lisa D. Pfefferle[3], Robert L. McCormick[1], Seonah Kim[1,2]*

[1] Fuels & Combustion Science, National Renewable Energy Laboratory
[2] Department of Chemistry, Colorado State University
[3] Department of Chemical and Environmental Engineering, Yale University

Electronic Supplementary Information

S1. Supplementary Data - High-Temperature Combustion

S1.1. Flow Reactor Experiments – Detailed Results

Fig. S1 contains the details of the flow reactor experiment results shown in **Fig. 2**. While **Fig. 2** shows only carbon yields of hydrocarbons (HCs), here, the products were lumped into three groups: HCs, oxygenates (containing greater than two carbon), and CO/CO_2. This approach enabled us to effectively identify the effect of fuel structure on the reaction pathway and provide the contribution of hydrocarbon and oxygenate products on the sooting tendency.

The flow reactor results for di-*n*-amyl ether (DAE) are presented in **Fig. S1 (a)**. DAE began to be consumed above 850 K, forming HC products ranging from C_1 to C_5, as shown in the pie graph at 950 K. This initial reactivity is attributed to the C-O bond fission reactions following hydrogen abstraction, which can be inferred by the analogous reactivity of diethyl-, dipropyl-, dibutyl ethers.[1-5] The fuel consumption was accelerated at temperatures higher than 950 K, leading to a steeper increase in HC yields. At temperatures above 950 K, the C-C bond cleavage of HCs occurred, resulting in shorter chain HC. This is inferred by comparing the pie graph at 950 K and 1050 K; that is, C_4 and C_5 HCs were observed at 950 K, whereas C_2 species were dominant at 1050 K without any C_4 or C_5 products detected. Above 1050 K, a slight decrease in HC yields was observed, accompanied by an increase in the yields of CO/CO_2. Meanwhile, a scarce amount of oxygenates (mainly pentanal) was observed at all temperatures.

A similar analysis was carried out for 4-butoxy-heptane (4BH), as shown in **Fig. S1 (b)**. An extensive amount of 4BH consumption was observed along with the entire temperature range, which is thought to be initiated by the hydrogen abstraction and C-O bond fission reactions similar to DAE. However, the onset temperature of 4BH consumption was lower than 750 K, indicating its high reactivity in the high-temperature regime compared to DAE. The higher reactivity of 4BH leads to larger HCs and oxygenate yields than DAE in the 750 – 925 K range. As the temperature rises above 925 K, C-C bond cleavage becomes a dominant reaction, as inferred by the pie charts at 925 K and 1075 K; C_7 species dominate at 925 K, while only $C_1 – C_3$ species were observed at 1075 K. On the other hand, the oxygenates, most of which consist of butanal, began to decompose and are fully consumed at >1000K. The yield of CO/CO_2 increases until 950 K and fluctuates at higher temperatures, likely due to the varying yield of HCs, despite the experimental uncertainty at high temperatures.

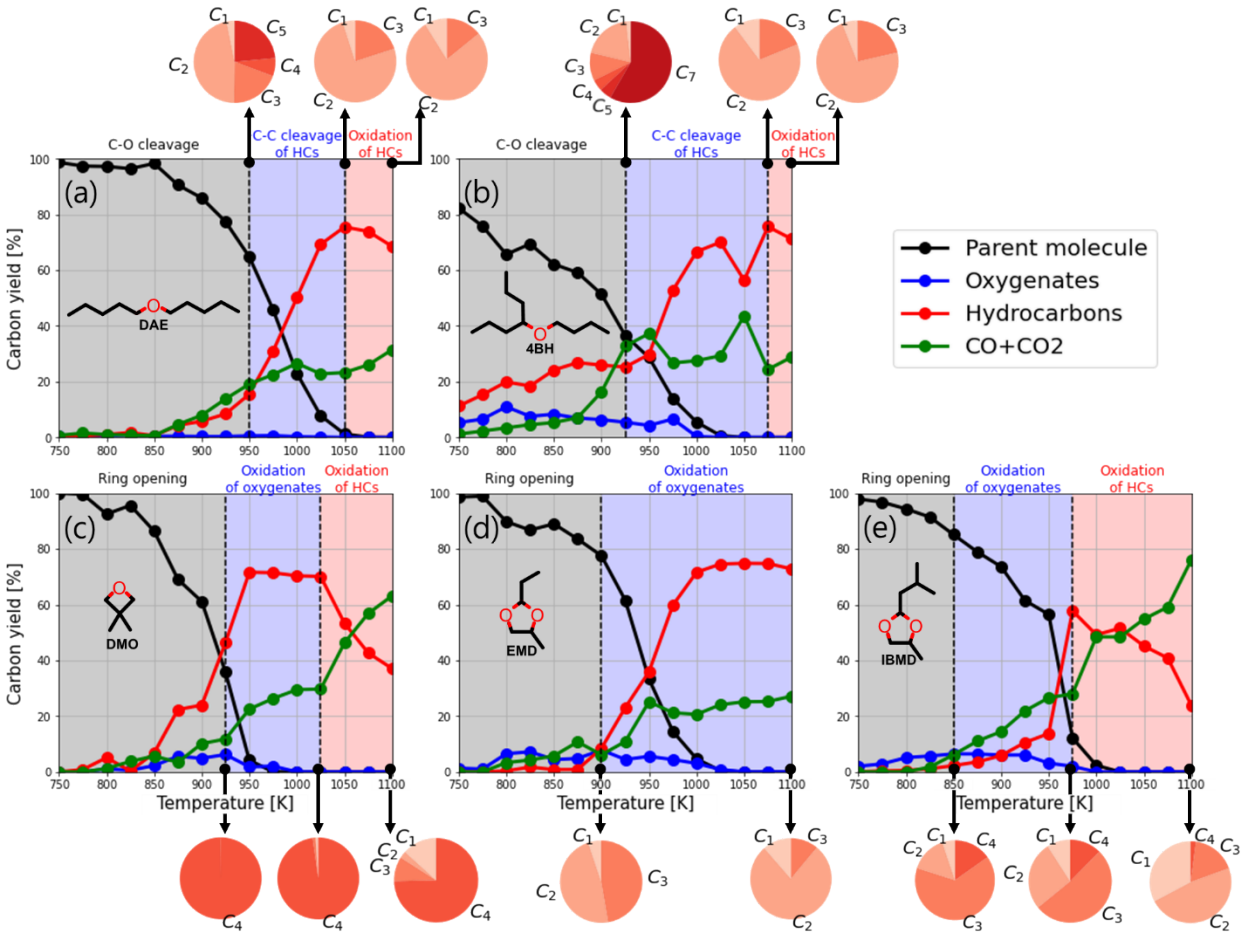

Fig. S1. The product distribution of (a) DAE, (b) 4BH, (c) DMO, (d) EMD, and (e) IBMD from flow reactor analysis performed from 750 – 1100 K, ϕ=3, at atmospheric pressure and residence time of 0.2 s. The pie chart shows the distribution of carbon numbers in HC products.

The products observed from the flow reactor experiment should play a key role in determining the soot formation in the flame. Considering that the YSI values increase as the number of carbons in the molecule increases,[6] it is a reasonable assumption that the YSI values of the fuel will be closely related to the size distribution of HCs from the high-temperature reaction, which is described with pie charts in **Fig. S1 (a)** and **S1 (b)**. At 1100 K, DAE and 4BH yielded a similar distribution of HC, but the portion of C_3 from DAE was slightly lower than 4BH. It is consistent with the slightly lower YSI/N_C value of DAE than 4BH (5.0 for DAE and 5.5 for 4BH).

The soot precursors formed from 3,3-dimethyl-oxetane (DMO) were investigated using the flow reactor, as depicted in **Fig. S1 (c)**. DMO started to decompose into HCs and oxygenates at 800 K. The majority (97%) of HCs produced were *iso*-butene, while all oxygenates were formaldehyde up until 1025 K. This strongly implies that the ring-opening reaction initiates the oxidation of DMO. It is comparable with the jet-stirred reactor experiment of Dagaut et al.[7] They measured the species profile from oxetane at 900 – 1150 K, atmospheric pressure, and stoichiometric condition and showed that predominately ethene and formaldehyde are produced. At 925 K, the DMO and HC yields reflected the vigorous ring-opening reaction, but the oxygenate

yield started to decrease. The loss of oxygenate yield can be understood as evidence of its oxidation, confirmed by the simultaneous increase in CO/CO_2 yield. At higher temperatures, around 1025 K, most of DMO decomposed, and HC oxidation started with the rise of CO/CO_2 yield. Comparing the size distribution of HCs at 925 K and 1025 K depicted in the pie charts shows that most of the HCs are C_4 species, mostly *iso*-butene, and its percentage barely changes with the oxidation of oxygenates. At 1100 K, it is evident that HC oxidation exhibits a remarkable effect on dissociating the C_4 species into C_1–C_3. Still, the size distribution of HCs from DMO oxidation was bigger than those of DAE, which is in line with its high YSI value (YSI/N_C=5.6). It should be noteworthy that the YSI/N_C of 4BH and DMO are comparable (5.5 vs. 5.6, respectively) despite of higher C_4 yields from DMO than 4BH. This may imply higher effectiveness of C_3 species for aromatic formation than C4 species, which is consistent with higher sooting tendency of propyne than iso-butene.[8]

The experimental results for 2-ethyl-4-methyl-1,3-dioxolane (EMD) are shown in **Fig. S1 (d)**. Most HC products were ethylene and propene (38 % and 55 % at 800K, respectively), while the oxygenates were mainly composed of propanal (79% at 800K). The acyclic structure of products implies the ring structure in EMD is opened at the early stage of its oxidation. The oxygenates products started to be oxidized at 900 K, which can be inferred by decreasing oxygenates yields and increasing CO/CO_2. The size of HCs at 900 K and 1100 K described in the pie chart of **Fig. S1 (d)** shows important features of EMD oxidation; that is, there are no C_4 compounds, while the C_2 and C_3 compound take the major portion (95 % at 900 K) of products contrary to DMO. Moreover, the relative portion of C_3 compounds decreased even further as temperature increased from 47 % at 900 K to 11 % at 1100 K. This smaller size distribution of HCs from EMD is consistent with the lower YSI value of EMD (YSI/N_C=4.0) than DMO (YSI/N_C=5.6).

The overall trend of 2-isobutyl-4-methyl-1,3-dioxolane (IBMD) oxidation from the flow reactor experiment was similar to EMD, as shown in **Fig. S1 (e)**. Its decomposition started around 800 K producing HCs and oxygenates; 63 % of the former is propene, and 63 % of the latter is 3-methyl butanal. It can be inferred from the acyclic structure of products that the ring-opening reaction occurs at the early stage of IBMD oxidation. As temperature increases over 850 K, we found that the oxygenates started to oxidize, but at a lower temperature than EMD (900 K). At 975 K, rapid decomposition of IBMD was observed with increasing HC yield. It was then followed by gradual oxidation of HCs beginning at 1025 K, contrary to the case of EMD, where no HCs oxidation was observed until 1100 K. One of the key differences between IBMD and EMD was the major component of oxygenates. IBMD primarily formed 3-methylbutanal, and EMD produced propanal, which must be attributed to the branched structure of alkyl substitution. The HC pie chart from IBMD across the three temperatures showed a higher concentration of C_3 and C_4 compounds than EMD, with the yield of C_3 and C_4 products decreasing with HC oxidation above 1000 K. Despite the HC oxidation, the size of HCs from IBMD was larger than EMD, which is consistent with the higher YSI value of IBMD (YSI/N_C=5.7) than EMD (YSI/N_C=4.0).

Comparing the size distribution of HCs from five tested fuels, we could find an interesting correlation between the size of HCs and the YSI/N_C. We hypothesized that the YSI/N_C of parent molecules might correlate with the carbon yield of C_3 and C_4 HCs products from the flow reactor experiment. We assumed the contribution of C_1 and C_2 species to YSI/N_C is marginal as the most C_1 and C_2 species observed in Fig. 2 are methane and ethylene, whose sooting tendency is much smaller than those of C_3 and C_4 alkene/alkyne. It should be noted that some C_2 species, such as acetylene (C_2H_2), can have a higher sooting tendency than C_3 and C_4 species. However, such high-

sooting C_2 HCs were not detected in the flow-reactor experiment of the present study; thus, assuming the low contribution of C_2 HCs is expected to be valid across the experimental conditions depicted in Fig. 2. The hypothesis can be expressed in the mathematical form as below:

$$YSI/N_C \sim X_{C3} + \alpha_{C4} X_{C4}$$

where X_{Cn} is the relative carbon yield of C_n HCs to the total HCs carbon yield at 1100 K. We introduced a scale parameter α_{C4} that has a physical meaning of the relative contribution of C_4 HCs to soot precursor formation compared to those of C_3 HCs. One reasonable estimation of α_{C4} would be the ratio of C_4's YSI to C_3's YSI, but the most recent database of YSI does not include C_3 or C_4 alkene/alkyne. Fortunately, the normalized smoke point (NSP), which is anti-proportional to the YSI,[6] is available for C_3 or C_4 alkene/alkyne.[8] The NSP of propyne and 2-butene (representative C_3/C_4 soot precursors) are 10.3 and 30.7, respectively. Of note, the NSP of ethylene is 120, showing the relatively low contribution of C_2 species to soot formation. We estimated α_{C4} as an inverse ratio of NSP of C_4 and C_3, which turned out to be $\alpha_{C4} \sim 10.3/30.7 = 0.34$. **Figure S2** shows a noticeable correlation between the suggested metric and YSI/N_C, while the DMO shows an outlying trend with a higher C_3 & C_4 portion than expected. The high C_3 & C_4 portion from DMO is attributed to the temperature range of the flow reactor experiment. The C_3 & C_4 portion was measured at 1100 K owing to the limitation of the flow reactor experiment, while the soot formation through polyaromatic hydrocarbon (PAH) growth from C_3 – C_4 HCs is most active around 1500 K.[9] As the temperature gets closer to 1500 K, the C_3 & C_4 portion from DMO is likely to decrease and lie in the trend in **Fig. S2**, as can be inferred from the decreasing HC size from 925 K to 1100K in **Fig. 2** of the manuscript. Based on the correlation between C_3 & C_4 portion and YSI/N_C, the following analysis focused on the underlying physics determining the size of HCs products from ether oxidation.

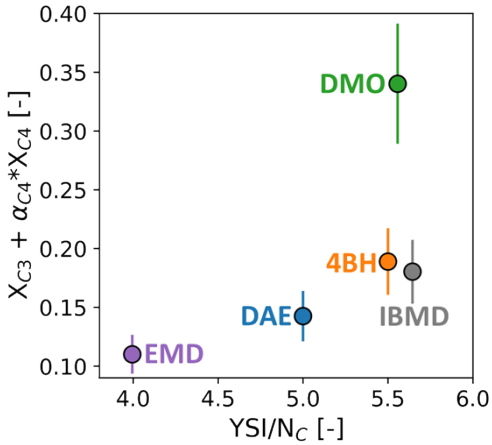

Figure S2 Correlation between the YSI/N_C and the C_3&C_4 portion in the HCs products.

Table S1. Kinetic parameters and reaction rates of benzene and fulvene formation from C_2, C_3, and C_4 hydrocarbons

Reaction type	Reactions[a]	A^b	n^b	$E_a{}^b$	$k^{b,c}$ @ 1100 K

$C_2 + C_4$	$C_2H_2 + C_4H_5 \rightarrow C_6H_6 + H$	1.36E-20	0.801	6348	2.04E-19
	$C_4H_3 + C_2H_2 \rightarrow C_6H_5$	2.66E-14	0.446	7719	1.84E-14
$C_3 + C_3$	$C_3H_3 + C_3H_5 \rightarrow$ Fulvene + H + H	9.23E-04	-2.535	1692	8.30E-12
	$C_3H_3 + C_3H_3 \rightarrow C_6H_6$	2.62E+31	-12.6	22300	4.65E-12

[a] Radical species (C_4H_5, C_4H_3, C_3H_3, and C_3H_5) and acetylene (C_2H_2) can be readily formed from hydrogen abstractions of butene (C_4H_8), propene (C_3H_6), and ethylene (C_2H_4) which were measured from flow reactor experiments. Hydrogen abstraction rates were omitted from the table since the C_2+C_4, and C_3+C_3 association reactions are rate-determining rather than hydrogen abstractions. [b] unit: cal, molecule, s, and K [c]Calculated using the modified Arrhenius equation: $k=AT^n\exp(-E_a/RT)$.

S1.2 Computational Mechanistic Studies - Detailed Results

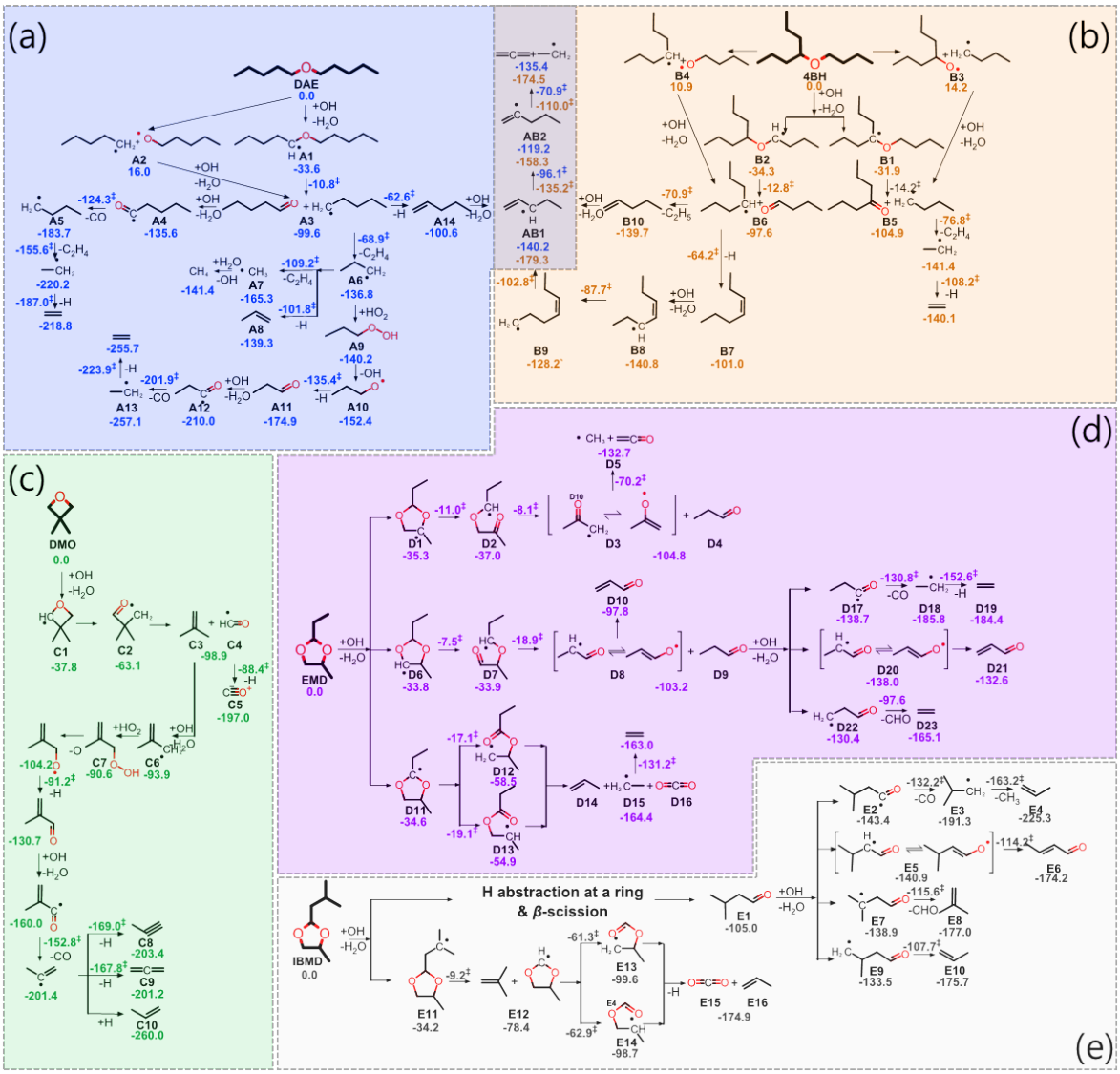

Fig. S3. Reaction pathway of (a) DAE, (b) 4BH, (c) DMO, (d) EMD, and (e) IBMD at the high-temperature regime, with relative free energies calculated at 1500 K using the G4 composite method (all units in kcal/mol). Relative free energies with respect to each parent

molecule were indicated with different colors: blue for DAE, orange for 4BH, green for DAE, purple for EMD, and gray for IBMD.

S1.2.1. Linear ether (DAE) vs. Branched ether (4BH)

As shown in **Fig. S3 (a)**, the decomposition of DAE was assumed to be initiated by hydrogen abstraction from the α-site, which is the most favorable C-H bond dissociation site, as was the case for diethyl-, dipropyl-, and dibutyl-ether.[1-5] It forms **A1** with the reaction free energy (ΔG) of -33.6 kcal/mol. Then, the β-scission reaction is expected to follow (**A1** → **A3**) to form a pentyl radical and pentanal with an energy barrier ($\Delta G^{\ddagger}$) of 22.8 kcal/mol. On the other hand, DAE can go through a direct dissociation of the C-O bond with a free energy cost of 16.0 kcal/mol (**DAE** → **A2**), followed by hydrogen abstraction to form pentyl radical and pentanal (**A3**). The pentyl radical undergoes the subsequent round of β-scission to produce propyl radical (**A3** → **A6,** $\Delta G^{\ddagger}$=30.7 kcal/mol), further decomposing into a methyl radical and ethylene (**A6** → **A7**, $\Delta G^{\ddagger}$=27.6 kcal/mol), or propene (**A6** → **A8**, $\Delta G^{\ddagger}$=27.0 kcal/mol). It can also go through the hydrogen abstraction ($\Delta G^{\ddagger}$=37.0 kcal/mol), leading to 1-pentene (**A3** → **A11**), which accounts for the formation of C_5 species.

Other possible pathways for the propyl radical (**A6)** include oxidation through the recombination reaction with HO_2 radicals. It should be noted that the oxidation can occur for any alkyl radicals (C_2 – C_5), although **Fig. S3 (a)** illustrates the propyl radical oxidation only. Along the oxidation pathway of HC, the hydroperoxide from the HO_2 + alkyl radical recombination reaction (**A6** → **A9**) was assumed to undergo the release of OH radicals to form an alkoxyl radical, making aldehydes through β-scission reaction (**A9** → **A10** → **A11**). Next, the additional hydrogen abstraction was assumed to occur by OH radical, leading to the formation of the acyl radical (**A11** → **A12**), which can readily release CO with an energy barrier of < 10 kcal/mol (**A12** → **A13**). The resulting alkyl radical then forms alkene through the C-H bond cleavage. All these β-scissions explain the production of ethylene as a major HC from DAE oxidation in **Fig. S1 (a)**. Meanwhile, the pentanal in **A3** can form an acyl radical right after hydrogen abstraction (**A3** → **A4**), releasing CO and butyl radicals (**A4** → **A5**). Carbon monoxide can undergo additional oxidation to form CO_2. Of note, all these pathways pertinent to the CO/CO_2 release occur with barrierless energies or $\Delta G^{\ddagger}$ < 10 kcal/mol for the CO release, indicating very rapid consumption of pentanal. This is in line with a scarce amount of pentanal in the experiment and a gradual increase of CO/CO_2 yield at all temperatures in **Fig. S1 (a)**.

The reaction energetics of DAE were compared with those of 4BH to explain their different YSIs; the reaction mechanisms of 4BH are shown in **Fig. S3 (b)**. There are two possible hydrogen abstraction sites adjacent to the ether oxygen; a tertiary and secondary carbon position, yielding a radical intermediate with the relative free energy of -31.9 and -34.3 kcal/mol (**B1** and **B2**, respectively). Next, β-scissions take place with $\Delta G^{\ddagger}$ of 17.7 and 21.5 kcal/mol (**B1** → **B5** and **B2** → **B6**, respectively). These barriers are lower than the β-scission barrier of DAE (22.8 kcal/mol). In addition, ΔG of the direct C-O fission reactions from 4BH (10.9 kcal/mol for **B3** and 14.2 kcal/mol for **B4**) is also lower than that from DAE (16.0 kcal/mol). All these energetics of the initiation steps align with the experimental results, which showed a higher C-O cleavage rate in 4BH than in DAE. The secondary carbon-oxygen bond cleavage from **B1** results in 4-heptanone and butyl radical (**B5**), while the tertiary carbon-oxygen bond cleavage from **B2** produces butanal and 4-heptyl radical (**B6**).

The further decomposition pathways of **B5** and **B6** were investigated; it is evident that the 4-heptanone in **B5** undergoes further reaction, as 4-heptanone was not observed in the flow reactor

experiments. Previous studies regarding the ignition pathways of C_3-C_5 ketones reported that hydrogen abstraction followed by β-scission reactions are most dominant.[10] Considering that their experimental conditions (1250 – 1850 K, ϕ=0.5-2.0) are relevant to soot precursor formation, we assumed that 4-heptanone is decomposed into C_3 species and carbon monoxide. On the other hand, the butyl radical in **B5** eventually forms two C_2 species through β-scission, which is in line with an increased C_2 formation at >1000K in **Fig. S1 (b)**. Possible decomposition pathways of **B6** include the formation of propyl radical and CO from butanal, analogous to the CO release from pentanal in **Fig. S3 (a)**. This explains the full consumption of oxygenates at >1000 K in **Fig. S1 (b)**.

For the subsequent reactions of 4-heptyl radical, either β-scission (**B6** → **B10**) or hydrogen abstraction (**B6** → **B7**) occurs with $\Delta G^{\ddagger}$ of 26.7 and 33.4 kcal/mol, respectively. The former releases ethyl radical and 1-pentene, whereas the latter forms 3-heptene (**B7**), which explains the C_7 species observed as a major product at 925 K (**Fig. S1 (b)**). One more hydrogen abstraction can occur at the allyl site of **B7**, which is favorable for stabilizing the resulting radical **B8**. Among many possible subsequent reactions of the allylic radical, here we investigated the internal hydrogen transfer (**B8** → **B9**) followed by β-scission (**B9** → **AB1**) to elucidate decomposition pathways of C_7 species at >925 K in **Fig. S1 (b)**. Each reaction occurs with $\Delta G^{\ddagger}$ of 53.1 and 25.4 kcal/mol, respectively, resulting in ethylene and pentenyl radical **AB1**.

1-pentene (**A14** and **B10**) is one of the common intermediates formed from both DAE and 4BH, and one should note that its formation from 4BH is thermodynamically and kinetically more favorable than that from DAE. In the case of DAE, the hydrogen abstraction from pentyl radical **A3** forms 1-pentene **A14** ($\Delta G^{\ddagger}$ = 37.0 kcal/mol), whereas in the 4BH pathway, $\Delta G^{\ddagger}$ of the β-scission of 4-heptyl radical (**B6** → **B10**) is only 26.7 kcal/mol. Moreover, the relative free energy of 1-pentene (**A14** and **B10**) from DAE and 4BH is -100.6 and -139.7 kcal/mol, respectively. These differences in energetics ultimately lead to a different extent of C_2 and C_3 species formation because allene and ethyl radical can be formed from 1-pentene via hydrogen abstraction, internal hydrogen transfer, and C-C fission (**AB1** → **AB2** → products, the shared pathway in **Fig. S3 (a)** and **3 (b)**).

The YSIs of DAE and 4BH can be explained based on the chemical kinetics and product distribution discussed above. 4-Heptyl radical and 3-heptene are formed only from 4BH, originating from the C-O bond fission around the branched structure. These species contribute to soot formation directly or through dissociation to produce C_3 HC products. Considering that two C_3 species can form benzene more rapidly than C_2 and C_4 species,[11, 12] the oxygenates and C_7 products from 4BH contribute to raising the soot concentration by producing more C_3 species. Moreover, the oxygenated intermediates, butanal, and 4-heptanone can also contribute to the formation of C_3 species. On the contrary, DAE can only produce propene from the β-scission of C_5 alkyl radicals. Therefore, the production of C_3 products from 4BH results in a higher YSI/N_C than DAE. To summarize, branched ethers have a higher YSI (and YSI/Nc) than linear ethers, likely due to (i) the higher C-O cleavage rate involving the tertiary carbon than the secondary carbon, and (ii) a higher reactivity of C_3 hydrocarbon formation.

S1.2.2. Linear ether (DAE) vs. Cyclic ether (DMO)

The underlying chemistry of the soot precursors produced from DMO was further analyzed using QM calculations, as shown in **Fig. S3 (c)**. First, DMO was assumed to decompose through the ring-opening reaction after H-abstraction, considering its weak bond dissociation free energy (44.1 kcal/mol for C-C ring bond and 42.0 kcal/mol for C-O ring bond). The QM calculation

revealed that the ring-opening reaction (**C1 → C2 → C3+C4**) is barrierless, generating *iso*-butene (**C3**) and formyl radical (**C4**). It is consistent with the observation from the flow reactor experiment in **Fig. S1(c)**, showing the abundant amount of C_4 species generation at the early stage of oxidation (<950 K). Then, **C3** and **C4** are expected to be oxidized into CO or smaller HCs. Although the oxidation pathways of both **C3** and **C4** showed a favorable energy barrier, the number of reaction steps and radicals required to be oxidized was much more complicated for the case of **C3**. For **C4**, the oxidation pathway is simple because it can directly form carbon dioxide through radical dissociation with the $\Delta G^{\ddagger}$ of 10.5 kcal/mole (**C4 → C5**). This reaction is expected to promptly occur because its exothermic energetics and marginal C-H bond energy of HCO radical enables the well-skipping reaction.[13] Meanwhile, **C3** must combine with HO_2 radical (**C3 → C6 → C7**) and go through subsequent reactions to be oxidized, forming various C_3 hydrocarbons (**C8** – **C10**). This is consistent with the higher temperature of HCs (**C3**) oxidation than the oxygenates (**C4**) observed from the flow reactor experiment (1025 and 925 K, respectively). In summary, the high stability of *iso*-butene from a ring-opening reaction of DMO is believed to contribute directly to shifting the size distribution of HCs to heavier (C_4), resulting in the high soot formation from DMO, as reflected by its YSI/N_C of 5.6.

S1.2.3. Oxetane (DMO) vs. Dioxolane (EMD)

Mechanistic studies on the soot precursor formation of EMD are shown in **Fig. S3 (d)**. The reaction was assumed to be initiated by hydrogen abstraction reaction at the weakest C-H bond, located at the carbon adjacent to oxygen atoms. This assumption is based on the reaction flux analysis on dioxolane at 850 K 10 bar in a jet-stirred reactor from Wildenberg et al.,[14] showing 98 % of dioxolane initiates the reaction by detaching the hydrogen from the α-site. Hydrogen abstraction leads to the formations of three fuel-radicals with different radical centers (**D1, D6,** and **D11**), all of which have a similar ΔG of around -35.3 – -33.8 kcal/mol. The **D1, D6,** and **D11** are then likely to decompose through β-scission reactions breaking a C-O bond. The $\Delta G^{\ddagger}$ of **D1** and **D6** decomposition were 25.3 kcal/mol and 26.3 kcal/mol, respectively (**D1 → D2** and **D6 → D7)**, while **D11** has a much lower energy barrier (15.5 – 17.5 kcal/mol). This should make the reaction flux to **D12** and **D13** favored, which makes propene (**D14**), ethyl radical (**D15**), and carbon dioxide (**D16**) through a barrierless reaction. This is consistent with the rapid increase of HCs and CO/CO_2 from 900 K, mostly comprised of C_2 or C_3 compounds, as shown in **Fig. S1 (d)**. On the other hand, **D2** and **D7** decompose to oxygenate compounds through subsequent β-scission reactions (**D2 → D3+D4**, and **D7 → D8+D9**), mainly producing ethenone (**D3 → D5**), propenal (**D8 → D10**), and propanal (**D9**) with $\Delta G^{\ddagger}$ of 28.9 and 15.0 kcal/mol, respectively. Propanal is a major oxygenate product from both **D2** and **D7** decomposition. This is consistent with the majority of propanal production from EMD decomposition (79% of oxygenates) observed from the flow reactor experiment (**Fig. S1 (d)**). Further mechanistic study on propanal (**D9**) revealed a plausible energy barrier to form C_2 compounds after hydrogen abstraction reaction: 33.2 kcal/mol for **D17 → D18 → D19** and 32.8 kcal/mol for **D22 → D23**. Therefore, the propanal contributed to the higher portion of C_2 concentration as it is dissociated around 900 K.

In summary, the ring-opening reactions from EMD are likely to generate oxygenates or a small (C_2 – C_3) hydrocarbon owing to the location of oxygen atoms. The size distribution of HCs even further shifts toward C_2 as propanal decomposes to the ethylene through oxidation. This high portion of C_2 compounds makes the EMD less likely to emit soot particles than the DMO, resulting in the low YSI value of EMD (YSI/N_C =4.0).

S1.2.4. Linear substitution (EMD) vs. Branched substitution (IBMD) in dioxolanes

The reaction pathway and corresponding energetics of IBMD are depicted in **Fig. S3 (e)**. Owing to their similarity, the overall reaction pathway of IBMD is similar to EMD shown in **Fig. S3 (d).** IBMD oxidation was assumed to be initiated by the hydrogen abstraction at the carbon adjacent to oxygen atoms and followed by the β-scission reaction breaking the C-O bonds in the ring. IBMD oxidation mostly results in the formation of 3-methyl butanal (**E1**), contrary to the propanal from EMD. This is in line with the observation of 3-methyl butanal from the flow reactor experiment, which takes up to 72 % of oxygenates compounds production at 750 K. Subsequent reaction of **E1** through hydrogen abstraction reaction and bond fission results in the formation of C_3 to C_4 compounds with plausible energy barriers: 28.1 kcal/mol for **E2 → E3 → E4**, 23.3 kcal/mol for **E7 → E8**, and 25.8 kcal/mol for **E9 → E10**. Additionally, the C-H bond at the tertiary carbon in the substituted alkane can be another channel of the hydrogen abstraction reaction of IBMD (**E11**). **E11** produces *iso*-butene and propene on the way of β-scission with $\Delta G^{\ddagger}$ of 25.0 kcal/mol (**E11 → E12 → E13 (or E14) → E15 + E16**), so it is another major source of C_3 to C_4 compounds. In summary, most of the reaction pathway from IBMD is similar to EMD, but the branched substation leads to the formation of branched aldehyde from the ring-opening reaction, which contributes to the production of C_3 to C_4 compounds. Moreover, the hydrogen abstraction from the tertiary carbon located in the substituted alkane can be an additional source of C_3 to C_4 HCs, causing IBMD to have a higher YSI value than EMD.

S2. The energetics relevant to the low-temperature chemistry of five tested fuels

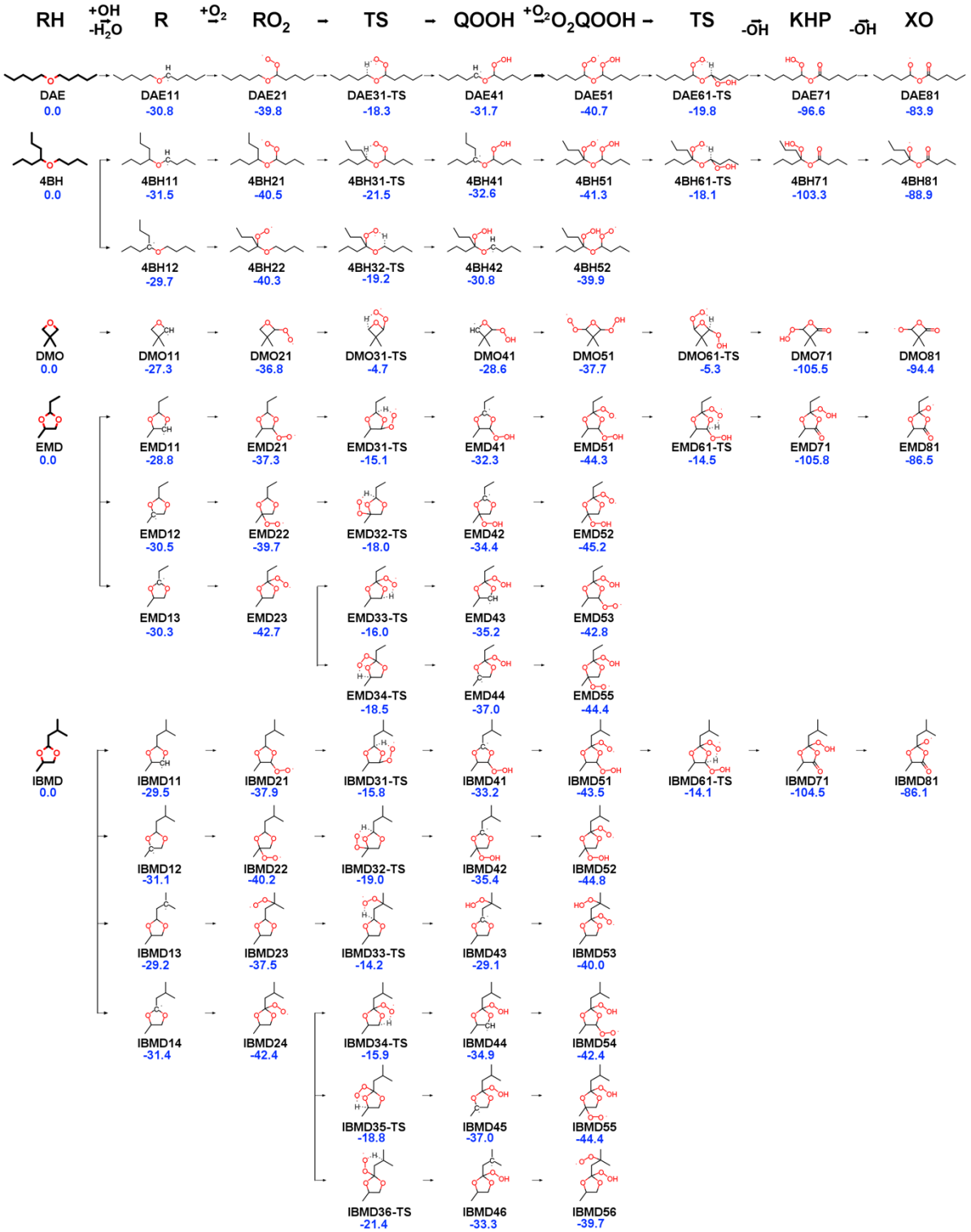

Fig. S4. The molecular structure and corresponding relative free energies of intermediates and transition states in low-temperature chemistry. The relative free energies were calculated at 700 K using the G4 composite method (all units in kcal/mol).

S3. The effect of carbon types on the energy barriers of low-temperature chemistry

For the RO_2 ↔ QOOH reaction in **Fig. S5 (a)**, differences of up to 6.0 kcal/mol were observed as the carbon type changed. The effect of carbon type on the A site was comparably small. However, the energy barrier was sensitive to the carbon type at site B (hydrogen atom donor). Having a tertiary carbon at site B lowers the energy barrier for hydrogen transfer compared to other carbon types and implies that the rate of RO_2 ↔ QOOH would be faster. This trend was observed when comparing DAE and 4BH in **Fig. 3**. When it comes to O_2QOOH ↔ KHP + OH in **Fig. S5 (b)**, up to 2.5 kcal/mol dependency was observed as the carbon type at the A site changes from primary to secondary carbon. Secondary carbon at both sites resulted in the lowest energy barrier (19.2 kcal/mol), which is in agreement with the previous DAE and 4BH comparison.

Fig. S5 (c) indicates the effect of ring strain on the energy barrier of RO_2 ↔ QOOH. It is obvious that the energy barrier increase as the ring strain on the participating carbon increases. Consequently, the maximal energy barrier (36.9 kcal/mol) was observed for the case with both carbons being in a 4-membered ring. The opposite case with both carbons being in the 6-membered ring showed the 16.1 kcal/mol lower energy barrier. This is consistent with the results in **Fig. 3**, where the cyclic ether (DAE, EMD, IBMD) compounds showed a higher energy barrier of RO_2 ↔ QOOH up to 13.2 kcal/mol than the acyclic compounds (DAE, 4BH).

It should be noted that the systematic analysis on O_2QOOH ↔ KHP + OH was not covered in this study. This is because searching for a minimal energy conformer was not straightforward as the slight difference in the molecular structure significantly impacts the intramolecular hydrogen transfer energy, especially for the cyclic structure. Nevertheless, the effect of the ring size is presumed to be large for O_2QOOH ↔ KHP + OH as it is a hydrogen transfer mechanism similar to RO_2 ↔ QOOH; we leave it for future work.

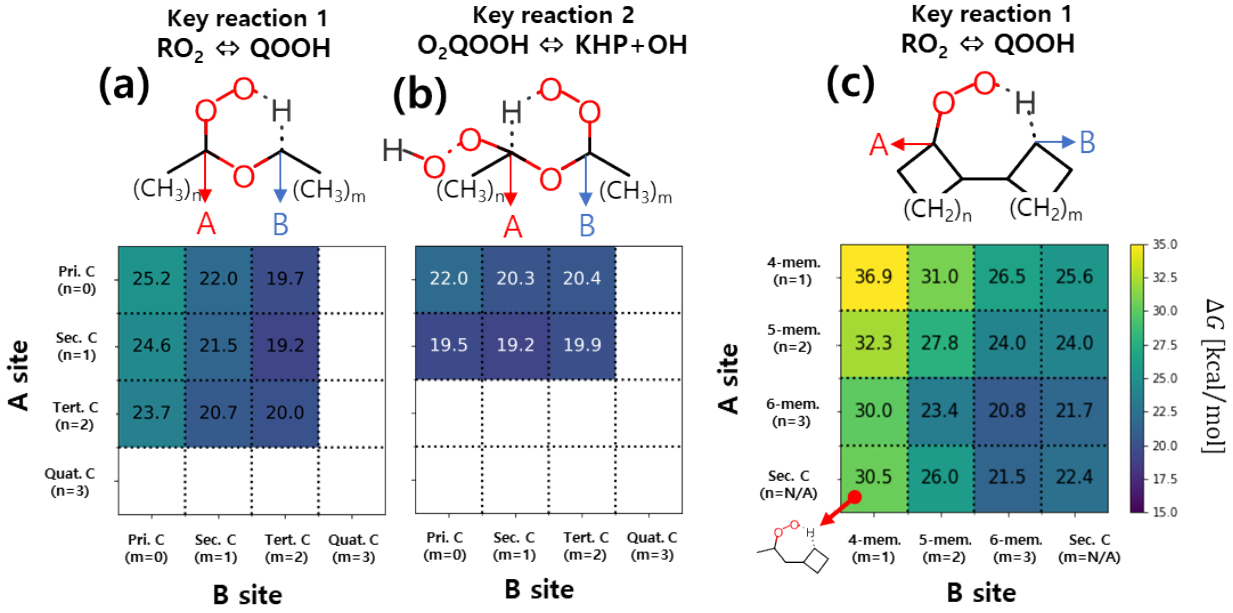

Fig. S5. Energy barriers of key reaction steps – (a) RO_2↔QOOH for acyclic structure, (b) O2QOOH↔KHP+OH for acyclic structure, and (c) RO_2↔QOOH for cyclic structure – with varying the carbon type or size of the ring.

S4. The effect of oxygen atoms on the low-temperature chemistry

Fig. S6 depicts how the energy barriers of post-QOOH reactions are dependent on the existence of oxygen atoms in the molecular structure. Each value and color in the grid indicates the difference between the energy barrier with and without oxygen atoms in the fuel; in other words, the negative values in the grid imply that the fuel with an oxygen atom (ether) has a lower energy barrier than otherwise (alkane). For the RO_2↔QOOH reaction (**Fig. S6 (a)**), the presence of an oxygen atom reduces the energy barrier up to -3.0 kcal/mol, but in some cases where both A site and B site are tertiary carbon, the energy barrier slightly increases by 0.5 kcal/mol. The energy barriers of O_2QOOH↔KHP+OH (**Fig. S6 (b)**) showed a similar effect of an oxygen atom, varying from -2.8 to -1.3 kcal/mol. Considering the G4 calculation has a 1.5 kcal/mol of uncertainty, the effect of oxygen atom indicated in **Fig. S6** is not sufficient to explain the role of ether functional groups in CN determination.

In this regard, we tested the effect of additional oxygen atoms on the thermodynamics of low-temperature chemistry. We employed a model fuel, 2-ethyl-5-methyl-tetrahydrofuran (EMTHF), which has a similar structure with EMD but has one less oxygen atom. Comparison between the overall energetics of low-temperature chemistry from EMD and EMTHF are depicted in **Fig. S7**. As we can expect from the results in **Fig. S7**, the EMD has only a slightly lower energy barrier than EMTHF up around ~ -3 kcal/mol. However, the thermodynamics of the EMD reaction showed much-favored energetics toward the formation of KHP, which is a key product promoting the chain branching reaction. It implies that the additional oxygen atom has a role to play to stabilize the KHP (up to 19.7 kcal/mol), thus contributing to enhancing the low-temperature chemistry and CN of fuel.

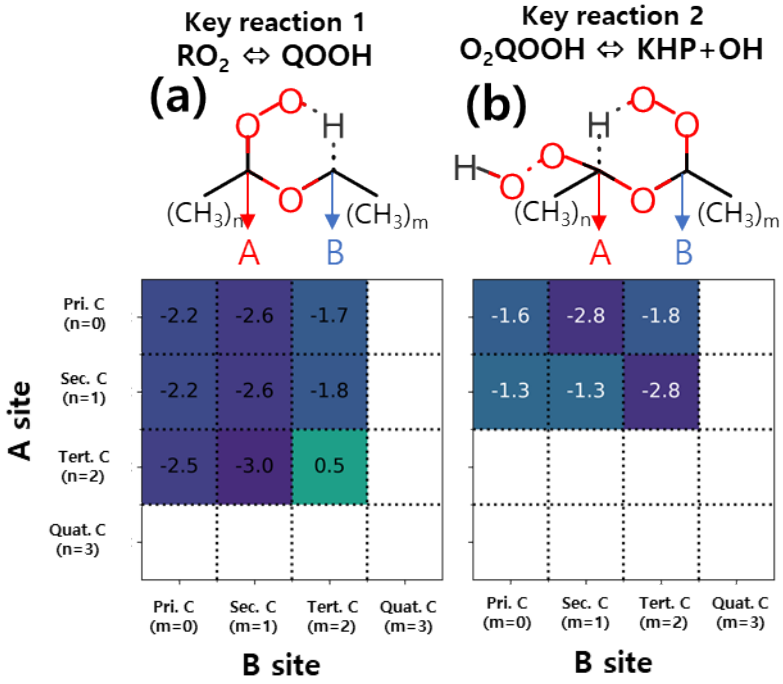

Fig. S6. The effect of oxygen atom in fuel on the energy barrier of key reaction steps – (a) RO2↔QOOH, and (b) O2QOOH↔KHP+OH – with varying the carbon type

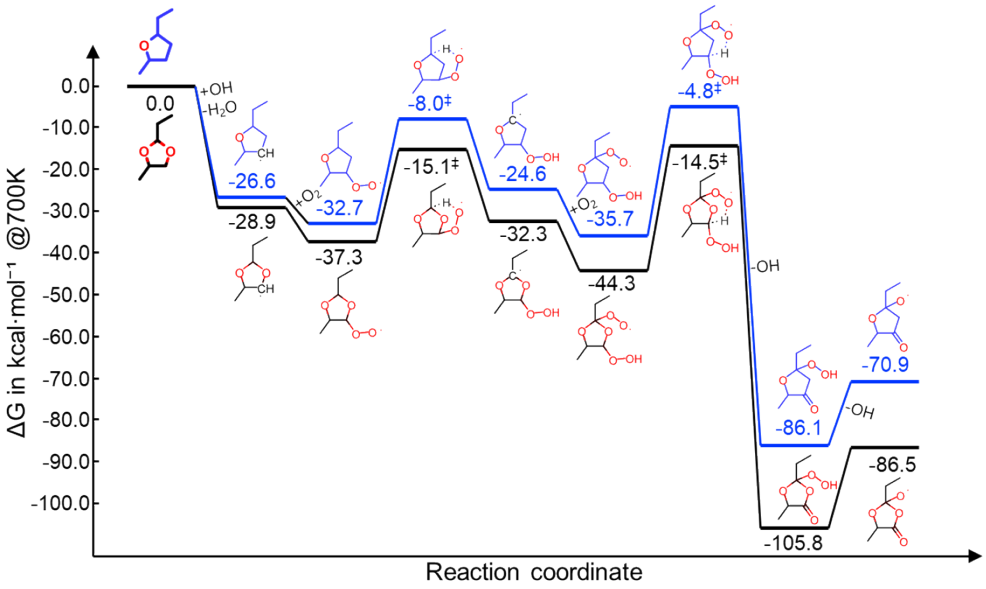

Fig. S7. Potential energy surface of low-temperature chemistry from EMD (in red) and EMTHF (in black)

S5. C-H bond dissociation enthalpies of ether molecules

The C-H bond dissociation enthalpies (BDEs) of five ether molecules were predicted using the ALFABET machine learning tool[15] to identify the carbons having weak C-H bonds, as shown in **Fig. S8**. For two acyclic ethers (DAE and 4BH), the carbon adjacent to the ether oxygen showed the lowest C-H BDE due to the radical stabilization by electron lone pairs of the oxygen atom. In 4BH, there are two different carbons bound to the ether oxygen; the tertiary carbon showed slightly higher BDE (94.0 kcal/mol) than the secondary one (92.8 kcal/mol), presumably due to the steric hindrance of two propyls during the hydrogen removal. Similar trends were observed for three cyclic ethers (DMO, EMD, IBMD); in DMO, the carbon next to the oxygen showed the lowest C-H BDE (95.0 kcal/mol). The three lowest BDEs were found in the three carbon atoms neighboring with two oxygens of the dioxolane rings of EMD and IBMD. In particular, the 4th weakest C-H bond of IBMD occurs at the tertiary carbon of the isobutyl group (94.5 kcal/mol) because of the stability of the tertiary carbon radical. The identified weak C-H bonds were used in the computational mechanistic studies of high-temperature (750 – 1100 K) and low-temperature (400 – 700 K) combustion pathways, as shown in **Figs. 2**, **3**, and **4** in Main Text.

It should be noted that many literatures have confirmed the dominance of the hydrogen abstraction from the weakest bond. Zhou et al.[16] calculated the theoretical rate constant of OH + various methyl ethers, including dimethyl ether (DME; C_2), ethyl-methyl ether (EME; C_3), and iso-propyl-methyl ether (IPME; C_4). The hydrogen abstraction from α-site carbon, which is adjacent to the oxygen atom, takes up ~ 90 % and ~ 80 % of the branching ratio at 1000 K for EME and IPME, respectively. Hu et al.[17] provided the theoretical rate constants of the diethyl ether (DEE; C_4) + OH, where the α-site abstraction is dominant with the branching ratio of ~ 95 % at 1000 K. For the larger ether molecules, the theoretical rate constant is only available for HO_2 + butyl-methyl ether (BME; C_5) and iso-butyl-methyl ether (IBME; C_5),[18] both of which showed the branching ratio to the α-site abstraction over 95 %. Although the α-site abstraction becomes less dominant at the higher temperature, its dominance is expected to be valid in the temperature range of the present experimental study (400 – 1100 K).

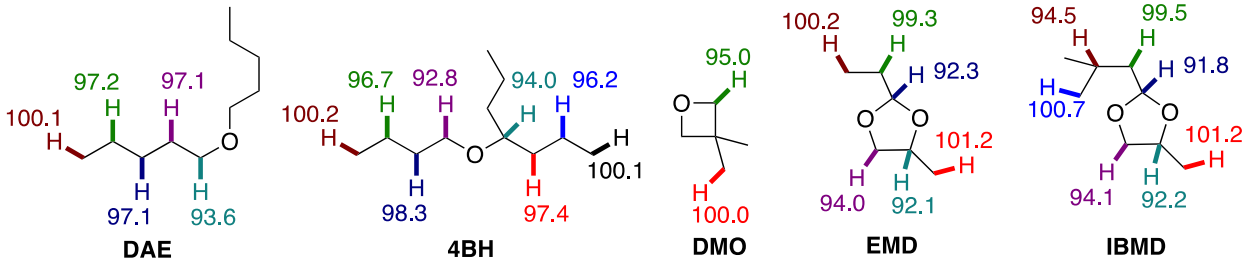

Fig. S8. C-H bond dissociation enthalpies (BDEs) of five ether molecules (kcal/mol). The BDEs were predicted using the machine learning tool (ALFABET) [ref]. DAE (di-n-amyl ether), 4BH (4-butoxy-heptane), DMO (3,3-dimethyl-oxetane), EMD (2-ethyl-4-methyl-1,3-dioxolane), IBMD (2-isobutyl-4-methyl-1,3-dioxolane).

S6. YSI & CN database

Table S2. YSI & CN database for 50 ethers

No.	SMILES	YSI_{exp}	YSI_{ML}	CN_{exp}	CN_{ML}
1	CCCCOC	23.0	-	-	61.2
2	CCCOCCC	28.0	-	-	65.3
3	CCCCOCCCC	38.7	-	-	-
4	CCCCCOCCCCC	49.8	-	111.0	90.2
5	COC(C)(C)C	31.5	-	-	9.9
6	CCOC(C)(C)C	37.9	-	-	14.6
7	CCC(C)(C)OC	38.1	-	-	16.8
8	CCC(C)OC(C)CC	54.0	-	-	46.1
9	CCCCOC(CCC)CCC	60.3	-	80.0	-
10	CCCCCC(CCCCC)OCC	68.5	-	-	91.6
11	CCCCCCOC(CCC)CCC	73.3	-	-	85.5
12	CC1(C)COC1	27.8	-	9.9	-
13	CCCCCCC1CCO1	52.7	-	-	64.6
14	CCCCCCCCC1CCO1	67.1	-	-	77.4
15	CCCCCCCCCCC1CCO1	78.9	-	-	87.0
16	CCCCCCC1(CC)CCO1	73.2	-	-	58.8
17	CCCCC1(CCCC)CCO1	74.7	-	-	53.0
18	CCCCCCCCCC1(C)CCO1	90.2	-	-	69.7
19	CCCCCC1(CCC)CCO1	87.5	-	-	54.3
20	CCCCC1(CCCC)COC1	89.3	-	-	64.9
21	C1CCOC1	20.1	-	21.9	-
22	CC1CCCO1	30.6	-	21.3	-
23	CC1CCC(C)O1	43.4	-	-	23.3
24	C1COCO1	10.3	-	-	22.2
25	CC1OCCO1	11.1	-	-	27.8
26	CC1(C)OCCO1	17.4	-	-	12.7
27	CCC1(C)OCCO1	21.1	-	-	15.5
28	CC1COC(C)(C)O1	25.6	-	-	12.4
29	CCC1OCC(C)O1	24.0	-	17.5	-
30	CCCC1OC(C)C(C)O1	36.5	-	33.4	-
31	CCCCCC1OC(C)C(C)O1	48.7	-	48.1	-
32	CCCCCCCC1OC(C)C(C)O1	63.2	-	68.9	-
33	CC(C)CC1OCC(C)O1	45.2	-	34.9	-
34	CCC(CC)C1OC(C)C(C)O1	57.8	-	44.8	-
35	CCCCC(CC)C1OC(C)C(C)O1	68.5	-	64.2	-
36	C1CCOCC1	26.5	-	38.2	-
37	CCCCCCOC	-	34.2	99.8	-

38	COCOC	10.9	-	49.0	-
39	COCCOC	11.8	-	81.0	-
40	CCOCOCC	18.5	-	57.3	-
41	CCOCCCCOCC	-	33.3	97.0	-
42	COCCCCCCOC	-	36.9	88.0	-
43	CCCCOCOCCCC	47.7	-	74.0	-
44	CCCOCOCCC	30.8	-	-	70.2
45	CCC(C)OC	28.6	-	38.3	-
46	CC(C)CCOCCC(C)C	63.6	-	85.1	-
47	CCC1CCCO1	-	37.0	28.1	-
48	CCCCC1CCCO1	-	49.8	45.5	-
49	CC(OC(C)C)C	38.7	-	-	33.0
50	CC(C)COCC(C)C	-	50.2	59.7	-

S7. Best-fit parameters from multivariate model

Table S3. Best-fit values and uncertainty of α_0 and β_0 in multivariate model

Parameter	Best-fit value
α_0	11.0 (±4.5)
α_1	4.7 (±1.0)
α_2	6.6 (±0.3)
α_3	11.8 (±2.1)
α_4	28.0 (±4.1)
α_5	0.3 (±1.9)
α_6	-1.6 (±1.5)
α_7	0.4 (±1.5)
α_8	7.2 (±2.7)
β_0	-18.6 (±7.6)
β_1	12.6 (±1.7)
β_2	8.5 (±0.5)
β_3	0.2 (±3.6)
β_4	-27.2 (±6.8)
β_5	27.7 (±3.3)
β_6	16.3 (±2.5)
β_7	-2.2 (±2.6)
β_8	29.9 (±4.6)

S8. Raw data from flow reactor experiment

Table S4. DAE oxidation at high-temperature (unit: C yield %)

Name	750K	775K	800K	825K	850K	875K	900K	925K	950K	975K	1000K	1025K	1050K	1075K	1100K
DAE	98.7	97.3	97.2	96.4	98.3	90.6	85.9	77.4	64.8	45.8	23.0	7.8	1.2	0.1	0.0
methane	0.0	0.0	0.0	0.0	0.0	0.1	0.1	0.2	0.5	1.0	1.7	2.7	3.6	4.9	6.1
ethane	0.0	0.0	0.0	0.0	0.0	0.1	0.1	0.2	0.6	1.3	2.3	3.7	4.8	5.8	6.3
ethene	0.0	0.1	0.2	0.4	0.2	1.2	1.9	3.0	6.7	15.5	27.8	42.5	49.7	49.8	46.1
propene	0.0	0.1	0.1	0.2	0.1	0.5	0.7	1.1	2.4	5.4	9.0	12.0	11.7	9.9	7.7
propyne	0.0	0.0	0.0	0.1	0.0	0.2	0.2	0.3	0.6	1.2	2.3	3.1	2.8	2.3	1.9
2-butene	0.0	0.0	0.1	0.1	0.0	0.2	0.4	0.6	1.1	2.3	3.6	3.9	2.6	1.2	0.3
2-propenal	0.0	0.0	0.0	0.0	0.0	0.0	0.0	0.0	0.0	0.0	0.0	0.0	0.0	0.0	0.0
2-pentene	0.1	0.4	0.7	1.0	0.3	2.0	2.3	2.9	3.7	4.3	3.4	1.4	0.3	0.0	0.0
pentanal	0.4	0.5	0.7	1.0	0.4	0.4	0.3	0.3	0.6	0.7	0.3	0.1	0.0	0.0	0.0
CO_2	0.7	1.6	1.0	0.8	0.6	3.2	5.1	8.9	12.1	15.2	17.0	13.7	12.6	13.6	14.3
CO	0.0	0.0	0.0	0.0	0.0	1.4	2.8	4.9	7.0	7.4	9.6	9.1	10.6	12.4	17.2

Table S5. 4BH oxidation at high-temperature (unit: C yield %)

Name	750K	775K	800K	825K	850K	875K	900K	925K	950K	975K	1000K	1025K	1050K	1075K	1100K
4BH	82.3	75.8	65.7	69.4	62.1	59.1	51.4	36.5	28.7	14.0	5.5	0.7	0.0	0.0	0.0
methane	0.0	0.0	0.0	0.0	0.1	0.1	0.2	0.4	0.9	1.5	2.0	2.7	4.1	4.5	7.2
ethane	0.0	0.0	0.0	0.0	0.1	0.2	0.4	0.9	2.1	4.2	5.9	7.5	8.6	9.2	8.9
ethene	0.0	0.1	0.2	0.2	0.6	1.1	2.1	4.0	9.8	18.8	30.5	36.1	33.6	44.8	41.2
propene	0.1	0.1	0.2	0.2	0.4	0.6	0.8	1.5	3.2	4.7	7.2	7.9	5.8	7.8	7.0
allene	0.1	0.2	0.1	0.1	0.5	0.7	1.0	1.3	1.9	7.1	10.8	11.5	3.0	8.1	6.3
2-butene	0.2	0.2	0.3	0.3	0.6	0.8	1.0	1.2	1.6	3.1	4.0	3.3	1.3	1.3	0.5
1-pentene	0.0	0.0	0.0	0.0	0.0	0.5	0.8	1.2	1.6	2.5	1.8	0.6	0.0	0.0	0.0
pentadiene	0.0	0.0	0.0	0.0	0.0	0.0	0.0	0.0	0.0	0.8	0.6	0.4	0.0	0.0	0.0
pentadiene	0.0	0.0	0.0	0.0	0.0	0.0	0.0	0.0	0.0	0.7	0.4	0.0	0.0	0.0	0.0
3-heptene	6.9	9.2	12.0	10.5	13.3	13.8	11.9	9.0	6.1	6.0	2.3	0.0	0.0	0.0	0.0

3-heptene	3.9	5.5	7.1	7.0	8.5	9.0	7.7	5.8	2.6	3.4	1.2	0.0	0.0	0.0	0.0
butanal	3.5	5.0	4.3	5.6	7.0	5.9	5.5	4.8	3.9	5.5	0.3	0.0	0.0	0.0	0.0
2-butenal	0.0	0.0	0.0	0.0	0.9	1.1	0.9	0.7	0.4	0.7	0.0	0.0	0.0	0.0	0.0
1-butanol	1.8	1.6	6.7	1.9	0.4	0.0	0.0	0.0	0.0	0.4	0.0	0.0	0.0	0.0	0.0
4-heptanone	0.0	0.0	0.0	0.0	0.0	0.0	0.0	0.0	0.0	0.0	0.0	0.0	0.0	0.0	0.0
CO_2	1.2	2.3	3.4	4.6	3.7	5.2	8.5	14.6	13.0	13.3	17.0	16.6	14.2	15.9	17.3
CO	0.0	0.0	0.0	0.0	1.7	1.9	7.8	18.2	24.3	13.4	10.5	12.7	29.4	8.5	11.6

Table S6. DMO oxidation at high-temperature (unit: C yield %)

Name	750K	775K	800K	825K	850K	875K	900K	925K	950K	975K	1000K	1025K	1050K	1075K	1100K
DMO	100.0	99.2	92.6	95.4	85.4	68.7	61.1	35.7	4.2	0.0	0.0	0.0	0.0	0.0	0.0
methane	0.0	0.0	0.0	0.0	0.0	0.0	0.0	0.0	0.1	0.2	0.2	0.6	8.1	1.8	4.9
ethane	0.0	0.0	0.0	0.0	0.0	0.0	0.0	0.0	0.0	0.0	0.0	0.1	2.1	0.4	0.3
ethene	0.0	0.0	0.0	0.0	0.0	0.0	0.0	0.0	0.0	0.0	0.0	0.1	0.0	0.1	0.7
propene	0.0	0.0	0.0	0.0	0.0	0.0	0.0	0.0	0.1	0.2	0.3	0.8	0.3	1.2	3.5
isobutene	0.0	0.8	5.1	0.3	6.7	22.3	23.9	46.3	71.3	71.1	69.9	68.7	43.0	39.3	27.6
formaldehyde	0.0	0.0	1.1	0.6	2.2	5.6	4.9	6.2	1.8	2.1	0.0	0.0	0.0	0.0	0.0
CO_2	0.0	0.0	1.2	3.8	5.6	3.4	4.8	5.7	16.1	17.1	23.2	23.0	19.3	23.5	23.1
CO	0.0	0.0	0.0	0.0	0.0	0.0	5.3	6.1	6.4	9.3	6.4	6.8	27.2	33.6	39.9

Table S7. EMD oxidation at high-temperature (unit: C yield %)

Name	750K	775K	800K	825K	850K	875K	900K	925K	950K	975K	1000K	1025K	1050K	1075K	1100K
EMD	98.6	98.9	89.8	86.8	89.0	83.5	77.5	61.6	33.3	14.6	4.7	0.5	0.0	0.0	0.0
methane	0.0	0.0	0.0	0.1	0.0	0.0	0.4	1.8	2.5	3.6	2.9	5.2	6.1	8.3	8.3
ethane	0.0	0.0	0.0	0.1	0.0	0.0	0.4	1.3	2.4	3.3	4.8	5.6	8.1	7.0	7.1
ethene	0.0	0.0	0.1	0.7	0.3	0.4	3.7	14.7	19.0	36.7	46.9	50.0	51.7	50.0	49.5
propene	0.0	0.0	0.2	1.0	0.4	0.4	4.0	5.3	12.0	16.2	17.0	13.9	8.9	9.4	8.0
formaldehyde	0.0	0.0	0.0	0.0	0.0	0.5	0.6	0.0	0.0	0.0	0.0	0.0	0.0	0.0	0.0
acetaldehyde	0.0	0.0	0.0	0.0	0.0	0.0	0.5	0.7	0.6	1.0	0.6	0.0	0.0	0.0	0.0
2-propenal	0.0	0.0	0.4	0.8	1.0	0.3	1.3	0.9	1.0	0.8	0.5	0.0	0.0	0.0	0.0

propanal	1.3	1.0	5.2	5.5	2.9	3.7	5.0	2.9	4.0	2.6	2.0	0.9	0.0	0.0	0.0
methyl oxirane	0.0	0.0	1.0	1.0	0.6	0.3	0.5	0.0	0.0	0.0	0.0	0.0	0.0	0.0	0.0
CO2	0.0	0.0	3.3	4.3	5.8	6.4	4.6	1.6	13.7	12.8	13.3	15.5	18.1	17.4	17.6
CO	0.0	0.0	0.0	0.0	0.0	4.4	1.5	9.3	11.5	8.4	7.4	8.6	7.0	7.8	9.5

Table S8. IBMD oxidation at high-temperature (unit: C yield %)

Name	750K	775K	800K	825K	850K	875K	900K	925K	950K	975K	1000K	1025K	1050K	1075K	1100K
IBMD	97.9	96.8	94.4	91.4	85.1	78.9	73.6	61.5	56.5	12.2	2.4	0.0	0.0	0.0	0.0
methane	0.0	0.0	0.0	0.1	0.1	0.2	0.3	0.6	1.1	5.3	4.3	4.6	9.5	14.3	7.8
ethane	0.0	0.0	0.0	0.1	0.2	0.3	0.5	1.0	1.0	4.1	5.8	8.5	8.6	7.5	8.5
ethene	0.0	0.0	0.0	0.1	0.1	0.2	0.4	0.9	1.3	11.4	8.4	8.9	8.8	7.2	2.9
propene	0.1	0.2	0.3	0.7	1.4	2.2	3.6	6.5	8.3	29.0	26.4	25.4	16.1	10.6	4.1
propyne	0.0	0.0	0.0	0.0	0.1	0.1	0.3	0.5	0.1	0.9	0.6	0.6	0.3	0.2	0.1
isobutene	0.0	0.1	0.1	0.2	0.3	0.5	0.8	1.1	1.9	7.1	3.8	3.5	1.9	1.1	0.5
acetaldehyde	0.0	0.0	0.0	0.0	0.0	0.0	0.4	0.5	0.6	0.6	0.0	0.0	0.0	0.0	0.0
2-propenal	0.0	0.0	0.0	0.0	0.4	0.6	0.8	1.2	0.0	0.0	0.0	0.0	0.0	0.0	0.0
propanal	0.6	0.8	1.3	1.5	1.8	1.8	1.7	0.9	0.7	0.4	0.0	0.0	0.0	0.0	0.0
methyl oxirane	0.0	0.0	0.5	0.6	0.7	0.7	0.6	0.7	0.0	0.0	0.0	0.0	0.0	0.0	0.0
3-methyl butanal	1.5	2.0	3.2	3.6	3.6	3.4	2.6	2.9	1.8	1.0	0.0	0.0	0.0	0.0	0.0
CO_2	0.0	0.0	0.0	1.7	4.4	9.3	11.5	16.3	19.0	18.4	18.5	16.0	15.5	18.5	22.1
CO	0.0	0.0	0.0	0.0	1.7	1.7	2.9	5.6	7.6	9.6	29.9	32.4	39.3	40.7	54.0

Table S9. DAE oxidation at low-temperature (unit: C yield %)

Name	400K	425K	450K	475K	500K	525K	550K	575K	600K	625K	650K	675K	700K
DAE	99.6	99.6	99.6	93.7	75.7	69.8	68.1	60.9	49.8	47.4	67.3	98.8	98.7
methane	0.0	0.0	0.0	0.0	0.0	0.0	0.0	0.0	0.0	0.0	0.0	0.0	0.0
ethane	0.0	0.0	0.0	0.0	0.0	0.0	0.0	0.0	0.0	0.0	0.0	0.0	0.0
ethene	0.0	0.0	0.0	0.0	0.1	0.1	0.1	0.3	0.8	1.3	0.7	0.0	0.1
propene	0.0	0.0	0.0	0.0	0.0	0.1	0.1	0.4	1.1	1.6	0.8	0.0	0.1
isobutene	0.0	0.0	0.0	0.0	0.1	0.2	0.3	0.8	1.5	2.0	0.8	0.0	0.0
2-pentene	0.0	0.0	0.0	0.0	0.0	0.0	0.2	0.6	1.4	1.9	1.8	0.1	0.1
formaldehyde	0.0	0.0	0.0	0.0	0.0	0.4	0.4	0.7	1.5	1.7	0.8	0.0	0.0
acetaldehyde	0.0	0.0	0.0	0.0	0.0	0.4	0.4	0.7	1.2	1.4	0.6	0.0	0.0
propanal	0.0	0.0	0.0	0.0	0.0	0.7	0.7	1.0	1.2	1.1	0.6	0.0	0.0
butanal	0.0	0.0	0.0	0.2	1.4	1.2	0.8	0.7	0.8	0.6	0.2	0.0	0.0
ethyl oxirane	0.0	0.0	0.0	0.0	0.0	0.4	0.5	0.8	1.5	1.6	0.6	0.0	0.0
2-pentenal	0.0	0.0	0.0	0.0	0.0	0.7	1.4	2.1	2.8	3.3	2.6	0.0	0.0
furan, tetrahydro-2-methyl-	0.0	0.0	0.0	0.0	0.0	0.0	0.3	1.0	2.9	4.6	4.0	0.1	0.1
pentanal	0.0	0.0	0.0	4.0	14.3	16.5	17.1	18.9	20.7	19.8	13.7	0.4	0.5
1-pentanol	0.4	0.4	0.4	0.5	0.7	1.2	2.0	2.7	3.1	3.2	2.5	0.3	0.3
pentanoic acid	0.0	0.0	0.0	1.2	3.1	2.3	1.5	1.0	0.8	0.4	0.2	0.0	0.0
$C_5H_8O_2$	0.0	0.0	0.0	0.0	0.4	0.4	0.4	0.4	0.5	0.4	0.1	0.0	0.0
formic acid pentyl ester	0.0	0.0	0.0	0.0	0.3	0.3	0.4	0.4	0.4	0.4	0.3	0.1	0.1
1-(ethenloxy)-pentane	0.0	0.0	0.0	0.0	0.3	0.6	0.8	0.9	1.0	1.0	0.7	0.0	0.0
pentanoic acid pentyl ester	0.0	0.0	0.0	0.4	1.3	2.0	2.1	2.4	2.4	1.8	0.6	0.0	0.0
CO_2	0.0	0.0	0.0	0.0	0.4	0.7	0.4	0.5	1.0	0.6	0.3	0.0	0.0
CO	0.0	0.0	0.0	0.0	1.8	2.0	1.8	2.6	3.7	3.8	0.8	0.0	0.0

Table S10. 4BH oxidation at low-temperature (unit: C yield %)

Name	400K	425K	450K	475K	500K	525K	550K	575K	600K	625K	650K	675K	700K
4BH	98.5	94.8	86.7	85.4	88.1	95.1	98.0	98.1	97.9	97.2	98.6	97.9	96.2

methane	0.0	0.0	0.0	0.0	0.0	0.0	0.0	0.0	0.0	0.0	0.0	0.0	0.0
ethane	0.0	0.0	0.0	0.0	0.0	0.0	0.0	0.0	0.0	0.0	0.0	0.0	0.0
ethene	0.0	0.0	0.0	0.0	0.0	0.0	0.0	0.0	0.0	0.0	0.0	0.0	0.0
propene	0.0	0.0	0.1	0.1	0.1	0.0	0.0	0.0	0.1	0.1	0.0	0.0	0.0
isobutene	0.0	0.0	0.0	0.0	0.0	0.0	0.0	0.0	0.0	0.0	0.0	0.0	0.0
1-pentene	0.0	0.0	0.0	0.0	0.0	0.0	0.0	0.0	0.0	0.0	0.0	0.0	0.0
3-heptene	0.0	0.0	0.0	0.0	0.0	0.0	0.0	0.0	0.2	0.3	0.2	0.4	1.1
3-heptene	0.0	0.0	0.0	0.0	0.0	0.0	0.0	0.0	0.0	0.2	0.2	0.3	0.9
propanal	0.0	0.4	0.5	0.4	0.0	0.0	0.0	0.0	0.0	0.0	0.0	0.0	0.0
butanal	0.0	0.7	2.5	3.0	2.5	0.9	0.3	0.3	0.5	0.4	0.1	0.0	0.2
1-butanol	0.0	0.0	0.0	0.0	0.0	0.1	0.0	0.0	0.0	0.0	0.2	0.4	1.0
butanoic acid	0.0	0.6	1.0	0.6	0.0	0.0	0.0	0.0	0.0	0.0	0.0	0.0	0.0
2-methyl-2,3-pentanediol	0.0	0.0	0.4	0.3	0.0	0.0	0.0	0.0	0.0	0.0	0.0	0.0	0.0
4-heptanone	0.0	1.3	3.9	4.8	3.8	1.8	0.6	0.5	0.7	0.5	0.2	0.2	0.2
4-heptanol	1.1	1.0	1.1	1.0	1.3	0.9	0.8	0.8	0.8	0.8	0.7	0.7	0.6
$C_7H_{10}O_4$	0.0	0.8	1.9	1.9	1.6	0.8	0.0	0.0	0.0	0.0	0.0	0.0	0.0
$C_7H_{10}O_4$	0.0	0.4	0.9	0.9	0.7	0.4	0.0	0.0	0.0	0.0	0.0	0.0	0.0
4-isopropyl 2,3-dihydrofuran	0.0	0.0	0.3	0.3	0.0	0.0	0.0	0.0	0.0	0.0	0.0	0.0	0.0
3-heptene-2-one	0.0	0.0	0.7	0.4	0.2	0.2	0.0	0.0	0.0	0.0	0.0	0.0	0.0
$C_8H_{16}O_2$	0.0	0.0	0.0	0.2	0.2	0.0	0.0	0.0	0.0	0.0	0.0	0.0	0.0

Reference

1. K. Yasunaga, F. Gillespie, J. Simmie, H. J. Curran, Y. Kuraguchi, H. Hoshikawa, M. Yamane and Y. Hidaka, *J. Phys. Chem. A*, 2010, **114**, 9098-9109.
2. N. Belhadj, R. Benoit, P. Dagaut, M. Lailliau, Z. Serinyel and G. Dayma, *Proc. Combust. Inst.*, 2021, **38**, 337-344.
3. S. Thion, C. Togbé, Z. Serinyel, G. Dayma and P. Dagaut, *Combust. Flame*, 2017, **185**, 4-15.
4. L.-S. Tran, J. Wullenkord, Y. Li, O. Herbinet, M. Zeng, F. Qi, K. Kohse-Höinghaus and F. Battin-Leclerc, *Combust. Flame*, 2019, **210**, 9-24.
5. Z. Serinyel, G. Dayma, V. Glasziou, M. Lailliau and P. Dagaut, *Proc. Combust. Inst.*, 2021, **38**, 329-336.
6. D. D. Das, P. C. S. John, C. S. McEnally, S. Kim and L. D. Pfefferle, *Combust. Flame*, 2018, **190**, 349-364.
7. P. Dagaut, M. Cathonnet, M. McGuinness and J. M. Simmie, *Combust. Flame*, 1997, **110**, 409-417.
8. L. Li and P. B. Sunderland, *Combust. Sci. Technol.*, 2012, **184**, 829-841.
9. Y. Xuan and G. Blanquart, *Combust. Flame*, 2013, **160**, 1657-1666.
10. H. Minwegen, U. Burke and K. A. Heufer, *Proc. Combust. Inst.*, 2017, **36**, 561-568.
11. C. J. Pope and J. A. Miller, *Proc. Combust. Inst.*, 2000, **28**, 1519-1527.
12. W. Tang, R. S. Tranter and K. Brezinsky, *J. Phys. Chem. A*, 2006, **110**, 2165-2175.
13. N. J. Labbe, R. Sivaramakrishnan, C. F. Goldsmith, Y. Georgievskii, J. A. Miller and S. J. Klippenstein, *J. Phys. Chem*, 2016, **7**, 85-89.
14. A. Wildenberg, Y. Fenard, M. Carbonnier, A. Kéromnès, B. Lefort, Z. Serinyel, G. Dayma, L. Le Moyne, P. Dagaut and K. A. Heufer, *Proc. Combust. Inst.*, 2020, **38**, 543-553.
15. P. C. S. John, Y. Guan, Y. Kim, S. Kim and R. S. Paton, *Nat. Commun.*, 2020, **11**, 1-12.
16. C.-W. Zhou, J. M. Simmie and H. J. Curran, *Phys. Chem. Chem. Phys.*, 2010, **12**, 7221-7233.
17. E. Hu, Y. Chen, Z. Zhang, J.-Y. Chen and Z. Huang, *Fuel*, 2017, **209**, 509-520.
18. J. Mendes, C.-W. Zhou and H. J. Curran, *J. Phys. Chem. A*, 2013, **117**, 4515-4525.